



## Hydroxyl time series and recirculation in turbulent nonpremixed swirling flames

Walter A. Guttenfelder<sup>a</sup>, Michael W. Renfro<sup>b</sup>, Normand M. Laurendeau<sup>a,\*</sup>, Jun Ji<sup>a</sup>, Galen B. King<sup>a</sup>, Jay P. Gore<sup>a</sup>

<sup>a</sup> School of Mechanical Engineering, Purdue University, West Lafayette, IN 47907-1288, USA

<sup>b</sup> Department of Mechanical Engineering, University of Connecticut, Storrs, CT 06269-3139, USA

Received 29 September 2005; received in revised form 22 July 2006; accepted 2 August 2006

### Abstract

Time-series measurements of OH, as related to accompanying flow structures, are reported using picosecond time-resolved laser-induced fluorescence (PITLIF) and particle-imaging velocimetry (PIV) for turbulent, swirling, nonpremixed methane–air flames. The [OH] data portray a primary reaction zone surrounding the internal recirculation zone, with residual OH in the recirculation zone approaching chemical equilibrium. Modeling of the OH electronic quenching environment, when compared to fluorescence lifetime measurements, offers additional evidence that the reaction zone burns as a partially premixed flame. A time-series analysis affirms the presence of thin flamelet-like regions based on the relation between swirl-induced turbulence and fluctuations of [OH] in the reaction and recirculation zones. The OH integral time-scales are found to correspond qualitatively to local mean velocities. Furthermore, quantitative dependencies can be established with respect to axial position, Reynolds number, and global equivalence ratio. Given these relationships, the OH time-scales, and thus the primary reaction zone, appear to be dominated by convection-driven fluctuations. Surprisingly, the OH time-scales for these nominally swirling flames demonstrate significant similarities to previous PITLIF results in nonpremixed jet flames.

© 2006 The Combustion Institute. Published by Elsevier Inc. All rights reserved.

*Keywords:* Hydroxyl; Integral time-scale; Swirling flames; Partial premixing

### 1. Introduction

Swirl in reacting systems can provide an increase in flame stabilization, as well as a reduction in flame length, owing to back-mixing with hot products. The resulting enhancement in ignition has been an important research topic for many years, especially

as related to fundamental mechanisms controlling swirling flows. For swirling flames, many variables can affect underlying interactions between turbulence and chemical reaction. The response of the flame to swirling flow is influenced by whether liquid or gaseous fuels are used, by the burner geometry, the method of swirl generation, fuel injection geometry, exit nozzle design, swirl number, Reynolds number, and the fuel-to-air momentum ratio.

A significant consequence of strong swirling flows is the establishment of a recirculation zone, which contains mean negative axial velocities. A nondimen-

\* Corresponding author. Fax: +1 (765) 494 0539.

E-mail address: [laurende@ecn.purdue.edu](mailto:laurende@ecn.purdue.edu)  
(N.M. Laurendeau).

sional swirl number,  $S$ , can be defined as a ratio of the axial flux of swirl momentum to a product of the axial flux of axial momentum and a characteristic length scale. A theoretical swirl number based solely on geometrical considerations can also be derived from this definition in order to obviate experimental information. For guide vanes in an axial tubular flow, which describes the configuration of this study, the theoretical swirl number,  $S_{th}$ , is [1]

$$S_{th} = \frac{2}{3} \left[ \frac{1 - (R_h/R)^3}{1 - (R_h/R)^2} \right] \tan \alpha,$$

where  $R$  is the swirler radius,  $R_h$  is the swirler hub radius, and  $\alpha$  is the vane angle with respect to the axis. Typically,  $S$  and  $S_{th}$  display adequate agreement, despite the fact that the above expression assumes thin vanes of constant chord and a uniform axial velocity distribution [1].

Beér and Chigier [1] claim that, for nonreacting swirling flows,  $S > 0.6$  is necessary to establish an internal recirculation zone. However, with the addition of heat release, recirculation zones can be established in flows having significantly smaller swirl numbers. Chen and Driscoll [2], for example, report a recirculation zone within a swirling flame with  $S = 0.2$ . Similarly, Tangirala et al. [3] find that a flame is necessary to induce recirculation in a flow with  $S = 0.7$ . The significant conclusion is that heat release increases the susceptibility of a flow to recirculation, as can be explained by considering the effects of density changes on pressure gradients [3].

The current study is aimed at utilizing picosecond time-resolved laser-induced fluorescence (PITLIF) to measure time series, and thus temporal statistics, of OH in nonpremixed, methane–air swirling flames. In this way, we add dynamic measurements of a reactive scalar to recent laser-induced fluorescence and Raman studies [4–6] in similar swirling flames. Our premise was that this first application of PITLIF to reacting flows with recirculation might lead to improved understanding of flame behavior in swirling flows. In general, the hydroxyl radical has been used extensively as a flame marker in nonpremixed and partially premixed flames; similarly, it is employed here to investigate in an approximate fashion the complex relation between chemical reaction and turbulence. In particular, temporal statistics for OH are investigated within regions of high turbulence intensity in swirling flames. Similarities are thus revealed between results from initially nonpremixed flames with recirculation and those from previous nonpremixed jet flames. To aid in understanding these OH measurements, mean and instantaneous flow structures are also investigated by implementing particle-imaging velocimetry (PIV).

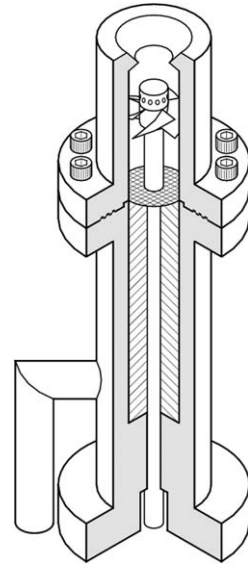


Fig. 1. Swirl burner of current investigation.

## 2. Experimental setup and procedures

The swirl burner employed for this study has the same geometry as that used by Cooper et al. [7] for heptane spray flames, but with a different fuel injector. The injector utilized here issues methane radially outward through 12 identical holes with diameters of 1.5 mm, as shown in Fig. 1. The swirler is an annular vane type, with vane angles of  $45^\circ$ , an overall vane radius of 11.5 mm, and a hub radius of 5 mm. The theoretical swirl number for this configuration is calculated to be  $S_{th} = 0.75$ . A  $40^\circ$  converging/diverging nozzle forms the exit of the burner, with a throat diameter of 12.7 mm.

Six atmospheric-pressure flames were considered in the present investigation. These nonpremixed flames were over-ventilated, with overall equivalence ratios ( $\Phi$ ) between 0.70 and 0.85 and Reynolds numbers ( $Re$ ) ranging from 12,600 to 42,100, based on total flow rates (methane and swirl air) and the nozzle throat diameter. These conditions were chosen so as to parametrically vary  $Re$  and  $\Phi$  while maintaining stable operation for our specific burner configuration. Table 1 gives the mean total velocity at the nozzle exit,  $U$ , for the flames considered in this investigation.

The flow structures within the swirling flames were obtained using cross-correlation, particle-imaging velocimetry (PIV). The PIV system arrangement and configuration are similar to those used by Ji et al. [8]. The CCD camera possesses frame-straddling capability, thus permitting times between two successive frames to be as short as 200 ns and providing up to 15 frame-straddled pairs per second, each

Table 1

Hydroxyl concentration statistics at locations of  $[\text{OH}]_{\text{max}}$ , as determined from time-series measurements in the six swirling flames

Re	$\Phi$	$x$ (mm)	$r_p$ (mm)	$[\text{OH}]_{\text{max}}$ ( $10^{-8}$ mol/cm <sup>3</sup> )	$[\text{OH}]_{\text{rms}}$ (%)	$\tau_{\text{avg}}$ (ns)	$I$ (%)
12,600 ( $U = 15.8$ m/s)	0.70	15	27	12.6	123	1.92	38
		30	31	10.6	163	1.90	38
		45	26	8.87	216	1.87	57
		60	22	5.69	288	1.86	82
		75	20	3.27	345	1.87	94
		90	0	0.88	262	1.89	99
16,800 ( $U = 21.1$ m/s)	0.70	15	31	10.9	125	1.90	39
		30	35	10.3	169	1.89	44
		45	37	10.3	227	1.89	72
		60	36	9.49	265	1.83	81
		75	28	6.06	328	1.81	91
		90	29	3.56	335	1.83	95
21,000 ( $U = 26.3$ m/s)	0.70	15	29	8.74	121	1.87	43
		30	36	9.48	143	1.83	32
		45	37	7.73	216	1.81	61
		60	35	5.46	293	1.72	83
		75	34	1.95	340	1.51	94
21,000 ( $U = 26.3$ m/s)	0.80	15	33	7.20	141	1.84	53
		30	42	7.73	170	1.89	50
		45	41	7.62	217	1.91	65
		60	40	6.04	274	1.88	85
		75	30	1.34	298	1.74	99
21,000 ( $U = 26.3$ m/s)	0.85	15	34	5.97	160	1.84	64
		30	38	6.32	189	1.87	64
		45	40	6.67	230	1.93	77
		60	34	6.64	276	1.89	88
42,100 ( $U = 52.6$ m/s)	0.70	15	36	6.37	189	1.89	68
		30	42	6.33	228	1.88	65
		45	42	4.66	277	1.93	72
		60	40	3.83	344	1.94	89
		75	42	3.22	382	1.88	96

*Note.* The mean exit velocity,  $U$ , is determined by the total flow rate at the nozzle throat diameter.  $[\text{OH}]_{\text{rms}}$  has been corrected for shot noise, as described in Ref. [11]. The parameters  $r_p$ ,  $\tau_{\text{avg}}$ , and  $I$  indicate the radial location of peak  $[\text{OH}]$ , the mean fluorescence lifetime, and the intermittency, respectively.

with an 8-bit output encompassing  $1000 \times 1016$  pixels. A double-pulsed Nd:YAG laser (400 mJ/pulse) with a wavelength of 532 nm operating at 10 Hz was used as the light source. An optical system with a planoconvex lens and a cylindrical–concave lens transforms the round laser beam into a laser sheet of about 1 mm thickness at the center of the measurement window. The CCD camera is oriented perpendicular to the laser sheet. A notch filter with a wavelength of  $532 \pm 3$  nm was used to minimize interference from flame radiation. A host computer captured more than 200 pairs of image frames continuously, with each frame covering a flow area of about 119 mm (width)  $\times$  121 mm (height). Aluminum oxide ( $\text{Al}_2\text{O}_3$ )

particles of 1–3  $\mu\text{m}$  were added to the air flow via a fluidized bed seeder. The captured particle images are processed using a two-frame cross-correlation function computed by fast Fourier transforms (FFT), with an interrogation box of  $32 \times 32$  pixels and a 50% overlap in each direction. The resulting spatial resolution for the flow-structure measurements is about  $3.8 \times 3.8$  mm.

The laser and optical systems for the PITLIF measurements were identical to those used by Renfro et al. [9]. Briefly, a mode-locked Ti:sapphire laser, with an 80-MHz repetition rate and a pulse width of 18 ps, is frequency-tripled to a wavelength of 309.33 nm, which excites the  $Q_1(8)$  line within the

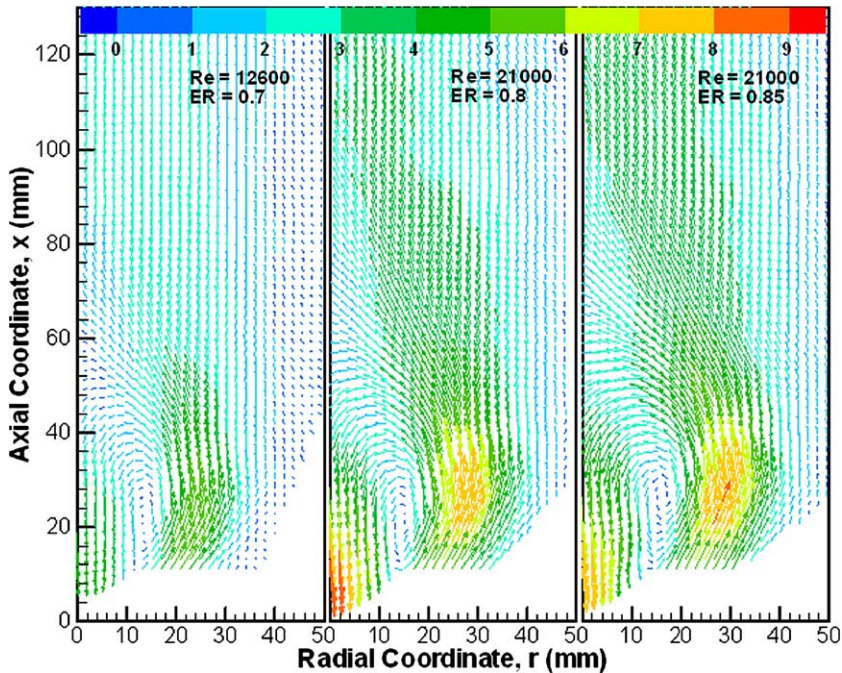


Fig. 2. Ensemble-averaged flow structures for three selected operating conditions.

(0, 0) vibrational band of the  $X^2\Pi-A^2\Sigma$  electronic system of OH. The incident laser beam is focused to a waist diameter of 108  $\mu\text{m}$ , which defines the diameter of the probe volume. The length of the probe volume is 125  $\mu\text{m}$ , as determined by the monochromator entrance slit and the detection optics. A 0.25-m monochromator filters the OH fluorescence at 309 nm with a 10-nm window. A PMT after the monochromator, in conjunction with a gated photon-counting system, permits determination of time series for the OH fluorescence lifetime, OH concentration, and background signal. The raw data from the photon-counting system are processed using a correction algorithm to account for system nonlinearities and saturation [10].

Radial profiles of mean OH concentration, fluorescence lifetime, and background emission were averaged over 3–8 s at a 10-Hz sampling rate. Time series were obtained by sampling 4096 data points at 25 kHz for all flames. Quantitative OH concentrations were calibrated against a well-characterized lean premixed  $\text{CH}_4$  ( $\Phi = 0.8$ ) flame on a McKenna burner [9]. Fifty consecutive time series were taken at each location, permitting suitable averaging of the temporal statistics. Probability density functions (PDFs) and auto-correlation functions were calculated for all data in each time-series set. Shot noise corrections were also performed for the autocorrelation functions, as described in Ref. [11].

### 3. Results and discussion

#### 3.1. Flow structure

Ensemble-averaged flow structures within the swirling flames for three selected operating conditions are shown in Fig. 2. Only half of the PIV measurements are displayed, owing to the symmetry produced by the swirl burner and its system arrangement. The magnitude of the velocity within the flow fields is color indexed in units of m/s. The internal recirculation zone can clearly be observed near the rim of the swirl burner in all three cases, as for the recent work of Weigand et al. [5]. Peak vorticities exist just outside the recirculation zone near the exit of the swirl burner. This toroidal recirculation zone becomes larger at higher Reynolds numbers. Moreover, the center of the recirculation zone shifts slightly away from the burner axis as the Reynolds number increases from 12,600 to 21,000. The center of the recirculation zone also moves downstream as the equivalence ratio (ER) rises from 0.80 to 0.85, while its radial location remains nearly fixed.

While ensemble-averaged flow structures gives some insight into flame stabilization in swirling combustion, instantaneous flow structures play a more crucial role in determining combustion stability, mixing enhancement, entrainment, ignition, and flame blowoff. In contrast to only a single internal recirculation zone for the ensemble-averaged velocity fields,

multiple but smaller vortices can be identified within the instantaneous velocity fields [8]. Furthermore, the highest magnitudes for the instantaneous velocity fields are much larger than those for the ensemble-averaged velocity fields of Fig. 2. Indeed, small intense but dynamic vortices are a dominant feature of swirling flows. At some locations, sudden enhancements in magnitude occur within the instantaneous velocity fields, which are not found for the mean velocity fields [8]. Strong flows normal to the measurement plane are necessary to support such enhancements, according to the requirements of mass conservation.

### 3.2. Mean hydroxyl profiles

Fig. 3 shows time-averaged radial profiles of hydroxyl concentration at axial heights ranging from 15 to 90 mm in the  $Re = 21,000$ ,  $\Phi = 0.70$  swirling flame, which are typical of all the flames of Table 1. Peaks in [OH] occur at locations between  $r = 30$  and  $r = 40$  mm from the burner centerline, consistent with the locus of peak mean temperatures along the outer dimensions of the recirculation zone [4], as shown in Fig. 2. Similarly, Masri et al. [4] previously established that the mean reaction zone, defined by  $\Phi_{\text{mean}} = 1.0$ , usually lies along the outer edge of the internal recirculation zone. The peak [OH] locations vary depending on the axial location in a given flame, but most remain far from the burner centerline. In comparison, toward the tip of the visible flames ( $x = 75$  to  $x = 90$  mm), the [OH] peaks approach the burner centerline, as also found by Masri et al. [4].

Table 1 provides radial locations ( $r_p$ ) for time-averaged  $[OH]_{\text{max}}$ , as determined from 10-Hz mea-

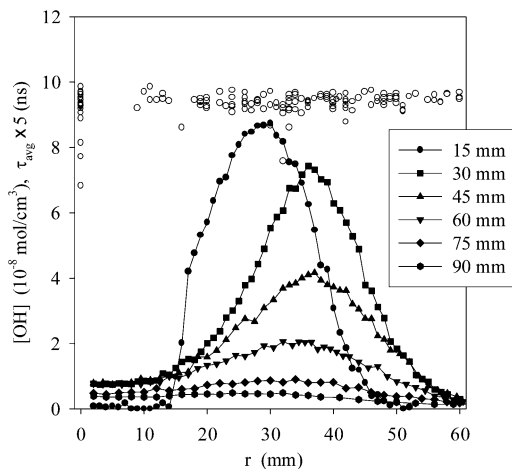


Fig. 3. Time-averaged radial [OH] profiles for the  $Re = 21,000$ ,  $\Phi = 0.70$  swirling flame (closed symbols) and mean fluorescence lifetimes,  $\tau_{\text{avg}}$ , for all flames (open symbols).

surements at each axial height for the six swirling flames. In general, the radial location corresponding to  $[OH]_{\text{max}}$  expands with higher Reynolds number, in line with stronger pressure gradients created from larger toroidal vortices at greater swirl velocities, as shown in Fig. 2. The flames are typically stabilized near the burner exit, upstream of the recirculation zone near the forward stagnation point, as postulated for both premixed [12] and nonpremixed [2,13] swirling flames. The forward stagnation point results in a localized low-velocity region with large pressure gradients that greatly enhances mixing. Planar laser-induced fluorescence (PLIF) images of OH in similar flames arising from annular fuel injection display a diverging OH zone immediately above the burner exit, consistent with rapid mixing along the high-temperature shear layer defining the edge of the internal recirculation zone [14]. Locations of  $[OH]_{\text{max}}$  in the present flames also diverge from  $x = 15$  to 30 mm, indicating that combustion is occurring around a central recirculation zone that is expanding from the burner exit. However, this divergence eventually decreases at downstream axial locations. Birouk and Gupta [15] present comparable OH PLIF images for lean-premixed swirling flames. Their images similarly suggest that the reaction zone largely surrounds the central recirculation zone, with stabilization again occurring very near the burner exit upstream of the recirculation region.

The mean OH concentration is essentially constant near the centerline, and typically 5–10 times smaller than at its radial peak for a given axial height (Fig. 3). The OH PLIF images of Cheng et al. [14] show some presence of OH in the recirculation zone for certain fuel-to-swirl-air ratios. The images of Birouk and Gupta [15] also indicate the presence of OH within the recirculation zone. Hydroxyl near the burner centerline might indicate either (1) an instantaneous reaction zone undergoing very large spatial fluctuations, or (2) a recirculation zone that provides, on average, a well-mixed environment of hot intermediates and products. The latter is more probable owing to the considerable amount of OH that mixes into the recirculation zone, as well as the rather slow three-body recombination reactions that subsequently eliminate OH [16]. Cheng et al. [14] report mean temperatures of up to 1600 K within the internal recirculation zone of similar swirling flames, which could be responsible for sustaining OH within this region despite its removal from the main reaction zone. Cooper et al. [4] report NO measurements in the same burner when using heptane introduced through a spray nozzle. The mean NO concentrations are constant near the burner centerline, again suggesting a uniformly mixed recirculation zone. At  $x = 15$  mm, OH is present along the centerline for the present flames, but only at the low-

est Reynolds number. The forward stagnation point of the recirculation zone is closer to the burner exit in this case because of its lower overall exit velocity, as depicted in Fig. 2.

The maximum hydroxyl concentration typically decreases as Reynolds number increases from  $Re = 12,600$  to  $42,100$ . For our conditions, this increase in  $Re$  occurs at the same fuel-to-air ratio ( $\Phi = 0.70$ ) and thus the overall flame structure expands outward, as previously explained by the increased size of the toroidal vortex. The resulting expansion in mean structure (see Fig. 2) leads to an increase in mixing with the surrounding, nonswirled air, providing a dilution effect at larger radial locations. At heights below  $x = 45$  mm,  $[OH]_{\max}$  also drops as  $\Phi$  increases from 0.70 to 0.85.

### 3.3. Basic hydroxyl statistics

Table 1 includes  $[OH]_{\text{rms}}$  values, mean OH fluorescence lifetimes ( $\tau_{\text{avg}}$ ), and intermittencies ( $I$ ) for the six swirling flames. The intermittency is defined here as the percentage of time OH is absent in the probe volume during the time-series measurements and is calculated using the measured PDFs. For all six flames, a strong inverse correlation exists between  $[OH]_{\max}$  and intermittency, implying that increased intermittency is partially responsible for the reduction in mean  $[OH]$ . However, the decrease in  $[OH]_{\max}$  with rising intermittency is less than that observed for jet flames [9], suggesting that both flame behavior and peak instantaneous  $[OH]$  values are also changing with axial height. Furthermore, peak instantaneous  $[OH]$  values are typically at least twice that of  $[OH]_{\max}$ , with the largest  $[OH]_{\max}$  values occurring lower in the flames. In particular, for the four  $\Phi = 0.70$  flames,  $[OH]_{\max}$  decreases steadily from  $x = 15$  to  $90$  mm. At greater overall equivalence ratios, however,  $[OH]_{\max}$  is nearly constant from  $x = 15$  to  $60$  mm, despite an increase in the accompanying intermittency. The implication is that local stoichiometric regions persist farther downstream with increasing overall equivalence ratio.

The  $[OH]_{\text{rms}}$  values reported in Table 1 are very large, ranging from 100 to nearly 400% of the mean. A strong correlation exists between the reported  $[OH]_{\text{rms}}$  and intermittency values in Table 1, with the highest rms and intermittency values occurring at greater axial locations. The larger OH intermittency can be attributed to two factors. First, the swirling flow exiting from the nozzle might lead to burning in the wrinkled-flamelet regime, as hypothesized to exist for turbulent diffusion flames and even in certain turbulent premixed flames. Convected flamelet behavior of this type would surely result in intermittent OH statistics, as OH is only measured when the flamelet

passes through the probe volume [9]. Alternatively, the intermittency could be a product of large-scale mixing that occurs within instantaneous flow structures [8]. Long, thin filaments of fuel could be rolled up between air and hot products into the internal recirculation zone [2]. Such instantaneous large-scale mixing would result in intermittent statistics, either from OH in the reaction zone or from OH in the hot products.

Further evidence for burning as thin filaments, possibly in the wrinkled flamelet regime, comes from recent OH- and CH-PLIF measurements by Weigand et al. [5] in stable swirling flames at  $\Phi = 0.55$ – $0.75$ . First, hydroxyl images show that  $[OH]$  occurs within and up to the inner edge of the internal recirculation zone, as expected for reactive or hot-gas mixtures. Second, single-shot OH and CH images indicate the existence of thin wrinkled reaction zones. In particular, the CH images identify clear fuel-consumption layers ( $<0.5$  mm), which are strongly corrugated and evidence flame extinction, similar to those of turbulent jet diffusion flames. In this case, however, locally unburned and extinguished regions within the recirculation zone probably originate from radial locations closer to the co-flow air [4]. Hence, the corrugated flame sheets persistently announce domination by the random turbulent flow field. Third, single-shot Raman measurements by Meier et al. [6] produce excellent correlations between temperature and  $[H_2O]$ , in agreement with strained laminar flame calculations. Similarly, Raman-derived scatter plots vs mixture fraction compare well with results from counterflow laminar flames [4]. Therefore, while not conclusive, evidence from this study, along with that from Refs. [4–6], strongly suggests laminar flamelet behavior.

The OH fluorescence lifetimes within the swirling flames of this investigation are approximately constant, independent of flame conditions ( $Re$  and  $\Phi$ ) and spatial location ( $r, x$ ). Fig. 3 displays mean OH fluorescence lifetimes measured in the six flames at all locations. Table 1 provides such lifetimes at positions of  $[OH]_{\max}$ . The average of all measured OH lifetimes is 1.87 ns with only a 4% standard deviation, which compares favorably with a mean repeatability in lifetime of 5% at a given location [17]. The few lifetimes that are smaller occur only in the  $Re = 21,000$ ,  $\Phi = 0.70$ , and  $\Phi = 0.80$ , flames at greater axial heights. We strongly suspect, however, that the worst case,  $\tau_{\text{avg}} = 1.51$  ns at  $\Phi = 0.70$  and  $x = 75$  mm, is an outlier, as explicitly indicated in Fig. 3.

Because burnout occurs in a relatively short length for swirling flames, entrainment of air cannot reduce OH temperatures sufficiently to produce larger quenching cross-sections and thus smaller fluorescence lifetimes. A similar quenching environment

was found for NO in swirling heptane–air flames using the same burner [7]. However, the NO measurements were obtained over a narrower radial region, typically within the internal recirculation zone where strong mixing tends to produce a constant quenching rate coefficient. The present OH measurements exist over a much broader region, well outside the internal recirculation zone and even extending beyond the visible reaction zone. For such conditions, we would expect within nonpremixed flames a variation in mean fluorescence lifetime of  $\pm 15\%$  ( $0.01 \leq Z \leq 0.12$ ) [18]. As a constant OH lifetime across all measured locations cannot be attributed to well-mixed conditions, we intuitively suspect the existence of partially-premixed combustion.

To gain further insight into the mixing field and the resulting quenching environment for the current swirling flames, predictions of the electronic quenching rate coefficient were made using simulated major species concentrations and quenching cross-sections from Paul [19]. The one-dimensional opposed-flow flame code OPPDIF [20] was employed, using GRI-Mech 3.0 [21], to simulate nonpremixed to partially premixed methane–air mixtures ( $\Phi_B = \infty$  to 0.77) flowing against air at a global strain rate of  $150 \text{ s}^{-1}$ . At the location of peak [OH], mole fractions for the major collisional quenching partners were used as inputs to the quenching model. The fit parameters for the species cross-sections were taken from Ref. [19], except for  $\text{H}_2\text{O}$ , whose fit parameters were determined by more recent simulations and measurements in laminar flames [22]. These  $\text{H}_2\text{O}$  cross-sections are about 15 to 25% larger than the cross-sections recommended by Paul [19], but they result in predicted fluorescence lifetimes that are in significantly better agreement with the experimental lifetimes of this investigation.

Fig. 4 shows the predicted fluorescence lifetimes at the location of peak [OH] based on the simulated species mole fractions and modified  $\text{H}_2\text{O}$  cross-section parameters. The predicted lifetimes decrease considerably with increasing burner-tube equivalence ratio ( $\Phi_B$ ) above the lean blowout limit, from 1.95 to 1.69 ns between  $\Phi_B = 0.77$  and  $\Phi_B = 1.06$ . This strong reduction when approaching  $\Phi_B = 1.0$ , as well as that when approaching from the rich side, can mostly be attributed to enhanced quenching via greater  $[\text{H}_2\text{O}]$ . In contrast, for  $\Phi_B \geq 1.2$ , the predicted fluorescence lifetimes show little variation, ranging between 1.77 and 1.88 ns, which comports well with the measured lifetimes of  $1.87 \pm 0.08$  ns. The relative invariance in predicted lifetimes for partially premixed flames ( $1.2 \leq \Phi_B \leq 5.0$ ) hints at the structure of the reaction zone in swirling flames. In particular, although the fuel is injected upstream of the exit nozzle and the region of flame stabiliza-

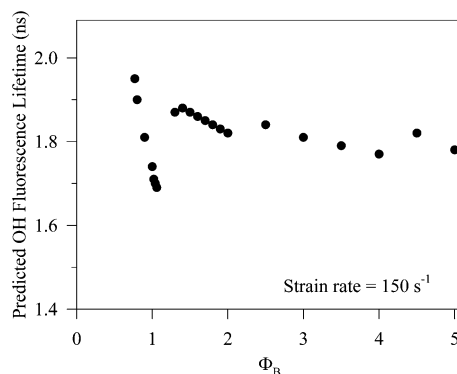


Fig. 4. Predicted OH fluorescence lifetimes at the location of peak [OH] for varying partially premixed flames. Lifetimes are determined using the “harpoon” mechanism for  $\text{OH}^2\Sigma^+$  collisional quenching [19], with mole fractions of major species predicted using OPPDIF [20] with GRI-Mech 3.0 [21].

tion, the constant measured lifetimes together with the above predictions suggest that full premixing is unachievable at the flame front. Moreover, laminar flamelets with varying degrees of partial premixing apparently duplicate the measured trends in OH fluorescence lifetime.

The implication of partial premixing based on fluorescence lifetime measurements in this investigation is substantiated by the recent work of Weigand et al. [5] and Meier et al. [6] on similar swirling flames. In their studies, partially premixed combustion was ascribed to flame stabilization above the nozzle, as verified by OH-PLIF images. Evidence comes from single-shot Raman measurements, which were found to produce mixture fractions less than unity ( $0 \leq Z \leq 0.2$ ) below the region of flame stabilization. Strong support also comes from the large number of Raman samples at 300 K, despite their being near stoichiometric conditions. According to Meier et al. [6], partial premixing in swirling flames can be attributed to a combination of local extinction and significant ignition delays owing to the large range of eddy compositions upon turbulent mixing. Therefore, from both laser Raman and PTLIF measurements, we conclude that partial premixing dominates in swirling flames, similar to that in turbulent jet flames with downstream stabilization.

### 3.4. Hydroxyl statistics from time series

Intermittency is clearly observable for most time series in these swirling flames, similar to previous OH measurements in nonpremixed jet flames [9]. Ultimately, for the latter, a flamelet concept was invoked to explain the resulting time series and their associated PDFs in terms of turbulent convection,

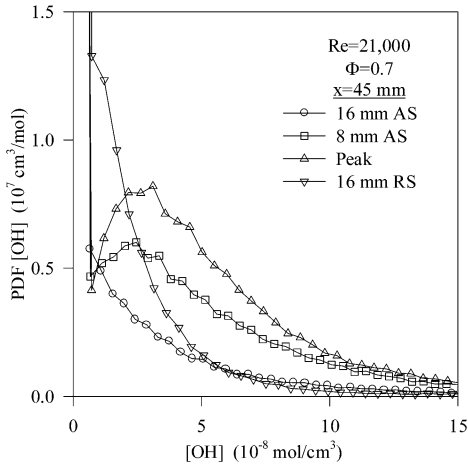


Fig. 5. PDFs for [OH] determined from time series in the  $Re = 21,000$ ,  $\Phi = 0.70$  swirling flame at an axial height of 45 mm on either the air side (AS) or the fuel side (FS) of the radial location for peak OH.

including predictions of the measured OH temporal statistics [23]. The OH intermittency in the present partially premixed flames suggests similar behavior. However, based on the mean [OH] profiles (Fig. 3), OH presumably exists away from the ensemble-averaged flame front and well into the internal recirculation zone. Furthermore, the instantaneous OH structures of Ref. [5] support OH intermittency within the recirculation zone; i.e., rapid large-scale mixing apparently produces the observed nonhomogeneous environment.

Fig. 5 shows PDFs calculated from the measured OH time series at a height  $x = 45$  mm above the burner surface in the  $Re = 21,000$ ,  $\Phi = 0.70$  flame. The PDFs at  $[OH]_{\max}$  and at 8 mm to either the reactive recirculation side (RS) or the entrained air side (AS) show similar distributions. In fact, the PDFs at the [OH] peak and at 8 mm to the air side have most probable values of [OH] that are nearly identical. Similar results were observed in previous nonpremixed jet flames across their mean [OH] radial profiles [9], thus providing further evidence for the presence of a convective flamelet structure. The PDFs near  $[OH]_{\max}$  are also comparable among these swirling flames, with absolute probabilities differing only because of changes in intermittency at a particular location within the flames.

At radial locations farther from  $[OH]_{\max}$ , the distributions of Fig. 5 shift toward much lower values of [OH]. On the air side of  $[OH]_{\max}$ , this change can be attributed to mixing with ambient air. The shift in distribution on the recirculation side arises from something different, at least at lower locations in the flame where little ambient air has been entrained into the internal recirculation zone. This lack of air entrain-

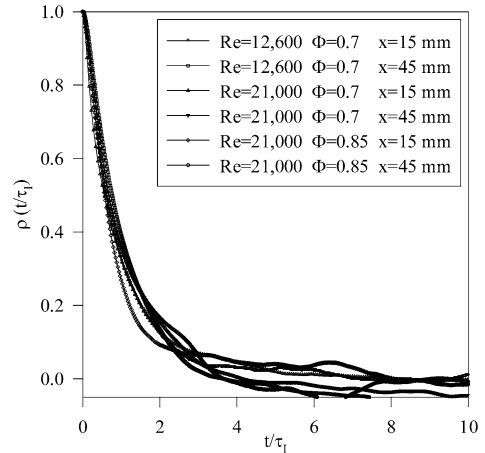
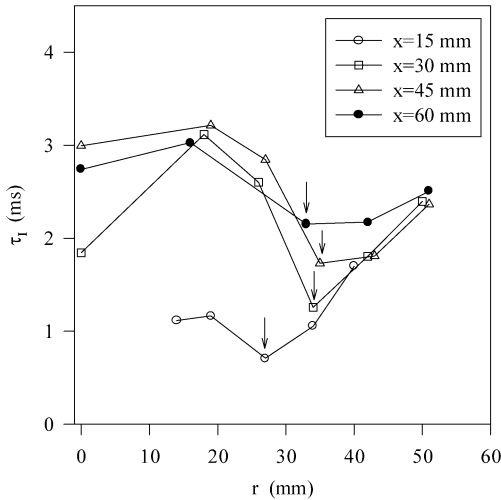


Fig. 6. Typical autocorrelation functions for the investigated swirling flames at the location of  $[OH]_{\max}$ , normalized by their respective integral time-scales.

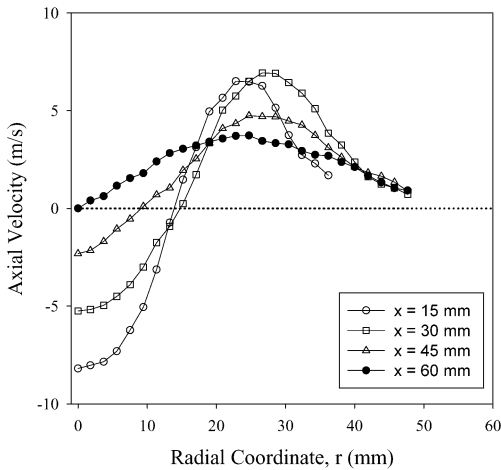
ment within the recirculation region has been shown by Chen [24] through visualization, and by Landenfeld et al. [25] through velocity measurements and Reynolds stress correlations. Hence, at such locations, OH tends to persist because of high temperatures, while being removed via slower three-body recombination reactions [16]. Therefore, the shift in OH distribution on the recirculation side likely results from [OH] approaching chemical equilibrium, consistent with longer residence times in the internal recirculation zone. For this reason, the OH shift is probably unrelated to flamelet motion into this zone.

Most autocorrelation functions determined from measured OH time series in the swirling flames display an approximately exponential decay. Upon integration, this simple shape provides a single computed integral time-scale,  $\tau_i$  [9], with a typical standard deviation of  $\sim 10\%$  [11]. Moreover, the autocorrelation functions are found to collapse when their respective time axes are scaled by these local time-scales, as shown in Fig. 6. This feature was previously observed for OH temporal statistics in turbulent nonpremixed jet flames [9], although the collapse for these swirling flames is not as complete at greater time delays. Nevertheless, because of the resulting self-similarity, scaling via integral time-scales appears warranted for most nonpremixed turbulent flames, whether jet or swirling.

A few autocorrelation functions, found only at  $x = 30$  mm in the  $Re = 12,600$ ,  $\Phi = 0.70$  and  $Re = 21,000$ ,  $\Phi = 0.85$  flames, exhibit much longer decay times and are not self-similar. These long correlation times indicate that [OH] is fluctuating relatively slowly. Along the centerline ( $r = 0$ ), relevant locations may correspond to slowly oscillating stagnation flow associated with the internal recirculation zone.



(a) Integral time scale



(b) Axial velocity

Fig. 7. (a) Radial profiles of OH time-scale for the  $Re = 21,000$ ,  $\Phi = 0.70$  swirling flame; (b) axial velocity profiles for the  $Re = 21,000$ ,  $\Phi = 0.80$  swirling flame. The arrows indicate the locations of  $[OH]_{\max}$  for each axial location.

Chen and Driscoll [2] and Halthore and Gouldin [12] suggest such behavior as a possible flame stabilization mechanism for their nonpremixed and premixed swirling flames, respectively. Farther from the centerline, long correlation times could correspond to lower mean velocities, as indicated in Fig. 2, while not necessarily being associated with the forward stagnation region. Larger correlation times may also be associated with broader OH distributions caused by enhanced vorticity or perhaps slower termolecular reactions promoting OH removal in the recirculation zone.

Fig. 7 displays radial profiles of the calculated integral time-scale for the  $Re = 21,000$ ,  $\Phi = 0.70$  flame and of axial velocity for the  $Re = 21,000$ ,

$\Phi = 0.80$  flame. Consistent dips appear in the integral time-scale for OH, which do not necessarily coincide with downstream peaks in axial velocity, as denoted by the arrows in Fig. 7a. The velocity profiles in Fig. 7b show that the mean axial velocity peaks near the ensemble-averaged flame zone at each downstream location, as would be expected from gas expansion [14,25,26]. More accurately, however, all dips in integral time-scale appear to be located outside their respective velocity peaks and nearer the location of peak mean  $[OH]$ . As usual, the smaller OH time-scales, corresponding to the primary reaction zone, result from enhanced turbulent convection, including a more frequent occurrence of OH intermittency.

The dependence of integral time-scale on radial position becomes more complicated nearer the centerline for all swirling flames of this investigation. Fig. 7a, for example, shows that OH time-scales at heights beyond the recirculation zone ( $x \geq 45$  mm) remain quite constant near the centerline; in comparison, an increase or decrease in integral time-scale occurs at lower heights. Specifically, at  $x = 30$  mm, a significant reduction in time-scale is evident near  $r = 0$  mm, where, as noted above, long correlation times are apparent for at least two swirling flames. Furthermore, considerably smaller time-scales are found toward the centerline at  $x = 15$  mm for all flames. At such lower heights, the integral time-scale corresponds to the upstream boundary of the recirculation zone, which approaches the forward stagnation point, as apparent from the mean  $[OH]$  profiles in Fig. 3. The forward stagnation region likely produces increased intermittency, thus introducing smaller integral time-scales.

By inspecting integral time-scales at locations of  $[OH]_{\max}$  ( $r_p$ ), a general trend can be observed for  $\tau_1$  vs  $x$ ,  $Re$ , or  $\Phi$ . Fig. 8 displays  $\tau_1$  at  $[OH]_{\max}$  plotted against axial position ( $x$ ) for various equivalence ratios at  $Re = 21,000$ . A near-linear relationship occurs between  $\tau_1$  and  $x$  for all three global equivalence ratios. A linear trend is also found if the same time-scales are plotted against equivalence ratio, perhaps owing to reductions in spatial OH width with rising  $\Phi$ . According to Beér and Chigier [1], the maximum axial velocity in a swirling jet scales with  $x^{-1}$ . Although data are sparse, axial velocity profiles reported for nonpremixed swirling flames [14,15] indicate similar decays in maximum velocity with axial position. However, because of combustion, entrainment of ambient air is less [24,25], and thus a smaller decay would not be surprising (see Fig. 7b).

As expected, the OH integral time-scale decreases with increasing Reynolds number. This behavior follows qualitatively convective scaling in turbulent flows. At most axial heights, a quantitative trend for time-scale vs  $x$  at the location of  $[OH]_{\max}$  can be

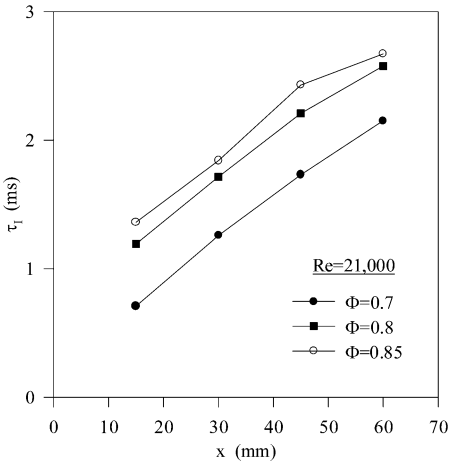


Fig. 8. Integral time-scales for OH determined at the location of  $[\text{OH}]_{\text{max}}$  plotted vs axial position for the  $\text{Re} = 21,000$  swirling flames.

reasonably approximated by a power law relationship, with a power index of approximately  $-0.7$ . This Reynolds number scaling is less than that reported for nonpremixed jet flames [9] or expected in nonreacting, convectively dominated flows. Hence, although a complex relationship exists between the OH integral time-scale and radial location, a reasonable approximation can still be made for the dependence of  $\tau_1$  at  $[\text{OH}]_{\text{max}}$  on  $\text{Re}$ ,  $x$ , and  $\Phi$ .

Finally, we have previously demonstrated that integral time-scales for OH can be directly related to those for mixture fraction through flamelet relationships [23]. These relationships make OH a suitable marker for mixing time-scales even though such time-scales are quantitatively different owing to the effects of intermittency [23]. For this reason, correlations of OH time-scales with Reynolds number, position, and equivalence ratio can be valuable as targets for unsteady flame simulations, including perhaps validations of large-eddy simulations [27].

#### 4. Conclusions

Time-series measurements of OH have been obtained for reacting flows with recirculation by employing picosecond time-resolved laser-induced fluorescence (PITLIF). Based on accompanying flow-structure measurements, the swirling flames include an internal recirculation zone, with peaks in mean OH concentration just outside this region. In addition, nonzero  $[\text{OH}]$  is found within the internal recirculation zone. Therefore, the measured OH arises from creation of  $[\text{OH}]$  near the edge of the recirculation zone, within the primary flame front, combined with sustenance of  $[\text{OH}]$  in high-temperature regions, de-

spite three-body recombination reactions that act to slowly remove the hydroxyl radical.

The measured OH fluorescence lifetimes indicate a constant quenching environment wherever OH is present, including across the mean reaction front and throughout the entire internal recirculation zone. Relatively short flame lengths prevent substantial mixing with cooler surrounding air, which would decrease fluorescence lifetimes. Quenching predictions based on OPPDIF simulations suggest that while all flames are over-ventilated with swirling air, local burning preferentially occurs as partially premixed flamelets, in agreement with recent laser Raman and PLIF measurements [5,6].

Intermittency is observed throughout all swirling flames, as indicated by the time series and the PDFs. This intermittency reflects flame motion, through both OH creation and sustenance. On this basis, thin instantaneous reaction fronts must exist at the edges and within the internal recirculation zone [5,6], which induce large-scale mixing of OH as its concentration approaches chemical equilibrium.

Nearly all autocorrelation functions calculated from the measured time series display an exponential decay; thus, they collapse to a single curve when normalized by their respective integral time-scales. Typical correlation times range from one to three milliseconds. A few autocorrelation functions exhibit significantly greater time-scales, typically at the forward stagnation point or near the center of the recirculation zone, where mean convective velocities are near zero.

The measured integral time-scales appear to be dominated by convection rather than by chemical reaction. In particular, the OH time-scales minimize axially at the peak of the mean  $[\text{OH}]$  profiles, just beyond the maximum velocity associated with the mean reaction zone. As expected, such time-scales increase with decreasing Reynolds number. Furthermore, integral time-scales measured at the location of  $[\text{OH}]_{\text{max}}$  display a positive linear dependence on both axial location and global equivalence ratio.

#### Acknowledgment

This work was supported by the Air Force Office of Scientific Research, with Dr. Julian Tishkoff as technical monitor.

#### References

- [1] J.M. Beér, N.A. Chigier, *Combustion Aerodynamics*, Wiley, New York, 1972, p. 112.
- [2] R.H. Chen, J.F. Driscoll, *Proc. Combust. Inst.* 22 (1988) 531.

- [3] V. Tangirala, R.H. Chen, J.F. Driscoll, *Combust. Sci. Technol.* 51 (1987) 75.
- [4] A.R. Masri, P.A.M. Kalt, R.S. Barlow, *Combust. Flame* 137 (2004) 1.
- [5] P. Weigand, W. Meier, X.R. Duan, W. Stricker, M. Aigner, *Combust. Flame* 144 (2006) 205.
- [6] W. Meier, X.R. Duan, P. Weigand, *Combust. Flame* 144 (2006) 225.
- [7] C.S. Cooper, R.V. Ravikrishna, N.M. Laurendeau, *Appl. Opt.* 37 (1998) 4823.
- [8] J. Ji, J.P. Gore, *Proc. Combust. Inst.* 29 (2002) 861.
- [9] M.W. Renfro, W.A. Guttenfelder, G.B. King, N.M. Laurendeau, *Combust. Flame* 123 (2000) 389.
- [10] M.W. Renfro, S.D. Pack, G.B. King, N.M. Laurendeau, *Appl. Phys. B* 69 (1999) 137.
- [11] M.W. Renfro, J.P. Gore, G.B. King, N.M. Laurendeau, *AIAA J.* 38 (2000) 1230.
- [12] R.N. Halthore, F.C. Gouldin, *AIAA J.* 24 (1986) 1129.
- [13] R.H. Chen, J.F. Driscoll, J. Kelley, M. Namazian, R.W. Schefer, *Combust. Sci. Technol.* 71 (1990) 197.
- [14] T.S. Cheng, Y.-C. Chao, D.-C. Wu, T. Yuan, C.-C. Lu, C.-K. Cheng, J.-M. Chang, *Proc. Combust. Inst.* 27 (1998) 1229.
- [15] M. Birouk, A.K. Gupta, *J. Heat Transfer* 120 (1998) 541.
- [16] R.S. Barlow, R.W. Dibble, J.-Y. Chen, R.P. Lucht, *Combust. Flame* 82 (1990) 235.
- [17] M.W. Renfro, G.B. King, N.M. Laurendeau, *Appl. Opt.* 38 (1999) 4596.
- [18] M.W. Renfro, S.D. Pack, G.B. King, N.M. Laurendeau, *Combust. Flame* 115 (1998) 443.
- [19] P.H. Paul, *J. Quant. Spectrosc. Radiat. Trans.* 551 (1994) 511.
- [20] A.E. Lutz, R.J. Kee, J.F. Grcar, OPPDIF: A Fortran Program for Computing Opposed-Flow Diffusion Flames, Sandia National Laboratories Report SAND96-8243.
- [21] G.P. Smith, D.M. Golden, M. Frenklach, N.W. Moriyarty, B. Eiteneer, M. Goldenberg, C.T. Bowman, R.K. Hanson, S. Song, V.V. Gardiner Jr., W.C. Lissianski, Z. Qin, GRI Mech 3.0, accessed October, 2001, available at: [http://www.me.berkeley.edu/gri\\_mech/](http://www.me.berkeley.edu/gri_mech/), 1999.
- [22] S.D. Pack, M.W. Renfro, G.B. King, N.M. Laurendeau, *Combust. Sci. Technol.* 140 (1998) 405.
- [23] M.W. Renfro, J.P. Gore, N.M. Laurendeau, *Combust. Flame* 129 (2002) 120.
- [24] R.H. Chen, *Combust. Sci. Technol.* 110–111 (1995) 443.
- [25] T. Landenfeld, A. Kremer, E.P. Hassel, J. Janicka, T. Schäfer, J. Kazenwadel, C. Schultz, J. Wolfrum, *Proc. Combust. Inst.* 27 (1998) 1023.
- [26] R. Hillemanns, B. Lenze, W. Leuckel, *Proc. Combust. Inst.* 21 (1986) 1445.
- [27] M.W. Renfro, A. Chaturvedy, G.B. King, N.M. Laurendeau, A. Kempf, A. Dreizler, J. Janicka, *Combust. Flame* 139 (2004) 142.